# Superconductivity in Cubic $La_3Al$ with Interstitial Anionic Electrons

Zhijun Tu(涂志俊)[1,2†], Peihan Sun(孙培函)[3†], Donghan Jia(贾东翰)[4], Huiyang Gou(缑慧阳)[4], Kai Liu(刘凯)[1,2*], and Hechang Lei(雷和畅)[1,2*]

[1]*School of Physics and Beijing Key Laboratory of Optoelectronic Functional Materials & MicroNano Devices, Renmin University of China, Beijing 100872, China*
[2]*Key Laboratory of Quantum State Construction and Manipulation (Ministry of Education), Renmin University of China, Beijing 100872, China*
[3]*Department of Physics, School of Science, Hebei University of Science and Technology, Shijiazhuang 050018, China*
[4]*Center for High Pressure Science and Technology Advanced Research, Beijing 100193, China*

(Received 13 December 2024; accepted manuscript online 16 January 2025)

We observed superconductivity in a cubic $La_3Al$ single crystal that exhibits metallic behavior in the normal state without an observable structural transition and enters the superconducting state below $T_c \sim 6.32$ K. Detailed characterization and analysis indicate that cubic $La_3Al$ is a bulk type-II BCS superconductor. Moreover, theoretical calculations show that it can host interstitial anionic electrons located at the body center of the cubic unit cell, which confirms electron–phonon coupling as the superconducting mechanism. Therefore, cubic $La_3Al$ can be considered as a novel electride superconductor.

DOI: 10.1088/0256-307X/42/2/027302 CSTR: 32039.14.0256-307X.42.2.027302

*1. Introduction.* Electrides are a unique class of materials in which electrons serve as anions.[1–3] These anionic electrons are mainly located in the interstitial positions rather than belonging to certain anions. Owing to the loosely bound nature of such interstitial anionic electrons (IAEs), electrides can exhibit many unique properties, such as low work functions,[4–6] high hyperpolarizabilities,[7] low-temperature thermionic emissions,[8] very strong reducibility,[9] and efficient catalytic activities.[10,11] These exotic properties of electrides have attracted significant interest for both fundamental science and practical applications. For example, electrides can be used as novel cathode materials for organic light-emitting diodes and as efficient catalysts for ammonia synthesis.[10,12,13]

In addition to their superior catalytic and electronic properties, some quantum properties such as magnetism, band topology, and superconductivity have also been predicted and discovered in electrides.[14–32] In particular, theoretical calculations have predicted that some electrides at high pressures can exhibit high superconducting transition temperatures $T_c$ beyond the McMillan limit ($\sim 40$ K) or even close to the temperature of liquid nitrogen. For example, hexagonal $Li_5N$ at 150 GPa and cubic $Li_8Au$ at 250 GPa are predicted to exhibit superconductivity at $T_c = 49$ K and 73 K, respectively.[24,25] Moreover, the cubic phase of Li formed above 41 GPa (space group $I\bar{4}3d$) is regarded as an electric superconductor with $T_c \sim 20$ K.[27,28] Thus, high-pressure electrides can be a novel platform for exploring high-temperature superconductivity. Compared to the intensively studied high-pressure electride superconductors, experimental studies on electride superconductors at ambient pressure have been rarely reported. For example, the inorganic electride $[Ca_{24}Al_{28}O_{64}]^{4+}\cdot 4e^-$ that exhibits superconductivity at $T_c \sim 0.4$ K[29–31] and $Nb_5Ir_3$ with one-dimensional IAEs that becomes superconducting below $T_c \sim 9.4$ K.[32]

Recently, we proposed that cubic $La_3In$ is a candidate electride superconductor with $T_c \sim 9.4$ K.[33] In this electride superconductor, the La and In atoms occupy the face-centered and vertex positions of the cubic structure, respectively. The IAEs are located at the body center of the cubic unit cell and surrounded by six La atoms. Cubic $La_3In$ belongs to the material family with a well-known $Cu_3Au$ structure (space group $Pm\bar{3}m$, No. 221) that includes thousands of binary compounds. Moreover, isostructural $La_3X$ (X = Ga, Sn, Tl) also shows superconductivity with $T_c \sim 5.8$–$9.0$ K.[34,35] Interestingly, $La_3Al$ exhibits two polymorphs. One has a hexagonal structure with an La Kagome lattice (space group $P6_3/mmc$, No. 194).[35,36] Hexagonal $La_3Al$ shows a superconductivity with $T_c = 5.80$–$6.37$ K.[35–37] Another polymorph of $La_3Al$ exhibits a cubic structure, isostructural to $La_3In$.[38] However, the physical properties of cubic $La_3Al$ remain unclear. In this study, we grew single cubic crystals of $La_3Al$ and studied their physical properties. We discovered that cubic $La_3Al$ exhibits superconductivity with $T_c \sim 6.32$ K. Further experimental and theoretical results indicate that cubic $La_3Al$ is an intermediately coupled type-II BCS superconductor with IAEs located at the centers of empty $La_6$ octahedra.

*2. Experimental and Calculation Details.* Single-

†These authors contributed equally to this work.
*Corresponding author. Email: kliu@ruc.edu.cn; hlei@ruc.edu.cn
© 2025 Chinese Physical Society and IOP Publishing Ltd. All rights, including for text and data mining, AI training, and similar technologies, are reserved.

crystals of $La_3Al$ were synthesized using the self-flux method. A chunk (purity 99.9%) and Al powder (purity 99.9%) were mixed at a molar ratio of 76 : 24. The mixture was loaded into an Nb crucible and sealed in a quartz ampoule under a partial argon atmosphere. The sealed quartz ampoule was heated to 1223 K for 24 h and soaked for another 24 h. Subsequently, it was cooled to 813 K at a heating rate of 2 K/h. Finally, the ampoule was removed from the furnace, and the $La_3Al$ single crystals were separated from the flux by centrifugation. The typical size of the $La_3Al$ single crystal is approximately $0.8 \times 0.8 \times 0.6\,mm^3$. X-ray diffraction (XRD) was performed using a Bruker D8 X-ray diffractometer with Cu $K_\alpha$ radiation ($\lambda = 1.5418$ Å) at room temperature. Single-crystal XRD patterns were obtained using a Bruker D8 VENTURE PHOTO II diffractometer with multilayer-mirror-monochromatized Mo $K_\alpha$ ($\lambda = 0.71073$ Å) radiation. Unit cell refinement and data merging were performed using SAINT, and absorption correction was applied using multiple scans. The composition of the $La_3Al$ single crystals was determined by examining multiple points on the crystals using energy-dispersive X-ray spectroscopy with an FEI Nano 450 scanning electron microscope. Electrical transport measurements were conducted using a superconducting magnetic system (Cryomagnetics, C-Mag Vari-9). Heat capacity and magnetization measurements were performed using a Quantum Design physical property measurement system (PPMS-14T) and magnetic property measurement system (MPMS3), respectively.

The electronic structures of $La_3Al$ were studied based on density functional theory calculations using the projector-augmented wave (PAW) method [39,40] implemented in the Vienna *ab initio* simulation package (VASP). [41–43] The generalized gradient approximation of the Perdew-Burke-Ernzerhof (PBE) type was adopted as the exchange-correlation functional. [44] The energy cutoff of the plane-wave basis was set to 520 eV. A $16 \times 16 \times 16$ Monkhorst-Pack $\boldsymbol{k}$-point mesh was used to sample the Brillouin zone (BZ). The Fermi surface was broadened using the Gaussian smearing method with a width of 0.05 eV. Both the lattice parameters and internal atomic positions were optimized. The convergence tolerances of the force and energy were set to 0.01 eV/Å and $10^{-5}$ eV, respectively. The maximally localized Wannier function method [45,46] was used to calculate the Fermi surface, which was visualized using the FermiSurfer package. [47]

To investigate the phonon spectra and electron–phonon coupling (EPC), density functional perturbation theory (DFPT) [48,49] calculations were performed using the Quantum ESPRESSO package. [50] The interactions between electrons and nuclei were described by the RRKJ-type ultrasoft pseudopotentials [51] from the PSlibrary. [52,53] The kinetic energy cutoff for the wavefunctions was set to 90 Ry. A Gaussian smearing method with a width of 0.004 Ry was used for the Fermi surface broadening. In the calculations of the dynamic matrix and EPC, the BZ was sampled using a $4 \times 4 \times 4$ $\boldsymbol{q}$-point mesh and a $60 \times 60 \times 60$ $\boldsymbol{k}$-point mesh, respectively. Based on the EPC theory, the Eliashberg spectral function $\alpha^2F(\omega)$ is defined as [54]

$$\alpha^2F(\omega) = \frac{1}{2\pi N(\varepsilon_F)} \sum_{\boldsymbol{q}\nu} \delta(\omega - \omega_{\boldsymbol{q}\nu}) \frac{\gamma_{\boldsymbol{q}\nu}}{\hbar\omega_{\boldsymbol{q}\nu}}, \tag{1}$$

where $N(\varepsilon_F)$ is the density of states (DOS) at Fermi level $\varepsilon_F$, $\omega_{\boldsymbol{q}\nu}$ is the frequency of the $\nu$th phonon mode at wave vector $\boldsymbol{q}$, and $\gamma_{\boldsymbol{q}\nu}$ is the phonon linewidth [54]

$$\gamma_{\boldsymbol{q}\nu} = 2\pi\omega_{\boldsymbol{q}\nu} \sum_{\boldsymbol{k}nn'} \left| g^{\boldsymbol{q}\nu}_{\boldsymbol{k}+qn',\boldsymbol{k}n} \right|^2 \delta(\varepsilon_{\boldsymbol{k}n} - \varepsilon_F) \delta(\varepsilon_{\boldsymbol{k}+\boldsymbol{q}n'} - \varepsilon_F), \tag{2}$$

where $g^{\boldsymbol{q}\nu}_{\boldsymbol{k}+\boldsymbol{q}n',\boldsymbol{k}n}$ is the EPC matrix. The total EPC constant $\lambda$ can be obtained using [54]

$$\lambda = \sum_{\boldsymbol{q}\nu} \lambda_{\boldsymbol{q}\nu} = 2 \int \frac{\alpha^2F(\omega)}{\omega} d\omega. \tag{3}$$

The superconducting transition temperature $T_c$ can be determined by substituting the EPC constant $\lambda$ into the McMillan-Allen-Dynes formula [55]

$$T_c = \frac{\omega_{\log}}{1.2} \exp\left[\frac{-1.04(1+\lambda)}{\lambda(1-0.62\mu^*) - \mu^*}\right], \tag{4}$$

where $\mu^*$ is the effective screened Coulomb repulsion constant ($\mu^* = 0.13$) and $\omega_{\log}$ is the logarithmically averaged phonon frequency.

$$\omega_{\log} = \exp\left[\frac{2}{\lambda} \int \frac{d\omega}{\omega} \alpha^2F(\omega) \ln(\omega)\right]. \tag{5}$$

*3. Results and Discussion.* As shown in Fig. 1(a), for cubic $La_3Al$, the La atoms are located at the face-centered positions of the cubic lattice, and the Al atoms occupy the vertex positions. The fit of the single-crystal XRD measurements at room temperature confirmed that the grown $La_3Al$ single crystal was in the cubic phase with lattice parameter $a = 5.0589(1)$ Å (Table 1). Based on the stoichiometric ratio of the atomic species in $La_3Al$, we deduced the existence of excess electrons in this material. Figures 1(a)–1(c) show the three-dimensional (3D) map for the electron localization functions (ELF), as well as the two-dimensional (2D) maps projected onto the (001) and (110) planes. As can be seen clearly, there are partial electrons separated from the nuclei and confined to the lattice cavities (center of empty $La_6$ octahedra), the so-called IAEs. [2,30,56,57] Based on the Bader charge analysis, each IAE carries a charge quantity of $0.53e^-$, functioning as a non-nuclear attractor with the capacity to attract electronegative atoms. [21,58] Hence, $La_3Al$ can be classified in the category of the well-known electride compounds. [1,60] In addition, the XRD pattern of the $La_3Al$ single crystal shows that all peaks can be indexed well by the ($h$00) diffraction indices of the cubic structure [Fig. 1(d)], indicating that the crystal surface is normal to the $a$-axis. The cubic shape of the $La_3Al$ crystal [inset of Fig. 1(d)] is consistent with the XRD pattern and its cubic crystallographic symmetry.

The temperature-dependent zero-field electrical resistivity $\rho_{xx}(T)$ of $La_3Al$ exhibited good metallic behavior and the residual resistivity ratio, defined as $\rho(300\,K)/\rho(6.5\,K)$, was approximately 8.2 [Fig. 1(e)]. Interestingly, when $T$ decreases to $\sim 55$ K, the $\rho_{xx}(T)$ curve

exhibits an anomalous kink. A similar anomaly has occasionally been observed in hexagonal $La_3Al$.[35–37] However, the results of single-crystal XRD measurements at $T = 40$ K indicated that there was no structural transition (Table 1). Thus, this anomaly may not originate from a structural transition, or the structural transition may be too subtle to be resolved using ordinary XRD. This resistivity anomaly requires further research. The $\rho_{xx}(T)$ curve between 7 and 48 K can be fitted well using the formula $\rho_{xx}(T) = \rho_0 + AT^n$; the obtained $n$ is 0.76(1), which is significantly different from the values due to conventional electron–phonon ($n = 5$) or electron-electron scattering ($n = 2$). On decreasing $T$ further, there is a sharp drop of resistivity at $T_c^{\rm onset} = 6.32$ K and $\rho_{xx}(T)$ becomes zero at $T_c^{\rm zero} = 6.11$ K, which is caused by superconducting transition [inset of Fig. 1(e)]. The $T_c$ value of cubic $La_3Al$ is close to that of the hexagonal structure ($T_c = 5.80$–$6.37$ K).[35,36] Figure 1(f) shows the magnetic susceptibility $4\pi\chi(T)$ curves measured at 1 mT in the zero-field cooling (ZFC) and field-cooling (FC) modes. Both curves exhibit a diamagnetic signal at $T_c^{\rm onset} \sim 6.22$ K, consistent with the $T_c$ value obtained from the $\rho_{xx}(T)$ curve. Moreover, the value of ZFC $4\pi\chi(T)$ approaches $-1$ after considering the demagnetization correction, clearly indicating the bulk superconductivity of cubic $La_3Al$ and excluding possible contamination of the hexagonal phase. The inset of Fig. 1(f) displays the $M(\mu_0 H)$ curve measured at 1.8 K, which shows obvious hysteresis. This suggests that cubic $La_3Al$ is a type-II superconductor, which is consistent with the bifurcation of ZFC and FC $4\pi\chi(T)$-curves below $T_c$.

Figure 2(a) shows the temperature dependence of $\rho_{xx}(T)$ at various magnetic fields up to 3 T. With an increase in the magnetic field, the superconducting transition broadens and $T_c^{\rm onset}$ gradually shifts to lower temperatures. When $\mu_0 H = 3$ T, no superconducting transition was observed above 2 K. The upper critical field

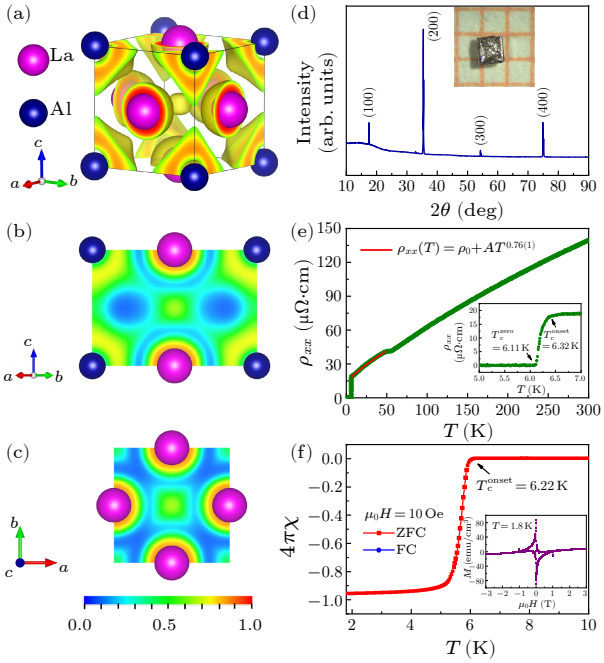


**Fig. 1.** Electron localization function (ELF) maps for $La_3Al$: (a) three-dimensional (3D) map, (b) and (c) two-dimensional (2D) map projected onto the (110) and (001) plane, respectively. The isosurface values were set to 0.5. The pink and blue balls represent La and Al atoms, respectively. (d) XRD pattern of a $La_3Al$ single crystal. Inset: photo of typical $La_3Al$ single crystal on a 1-mm grid paper. (e) Temperature dependence of $\rho_{xx}(T)$ at zero field for $La_3Al$ single crystal. Inset: Enlarged view of $\rho_{xx}(T)$ curve near $T_c$. (f) Temperature dependence of $4\pi\chi(T)$ of $La_3Al$ single crystal at $\mu_0 H = 1$ mT with ZFC and FC modes. Inset: isothermal magnetization loops at $T = 1.8$ K.

**Table 1.** Crystallographic data and atomic positions for $La_3Al$ at different temperatures.

| $T$ (K) | 40 | 100 | 300 |
|---|---|---|---|
| Space group | $Pm\bar{3}m$ | $Pm\bar{3}m$ | $Pm\bar{3}m$ |
| Crystal system | Cubic | Cubic | Cubic |
| $a$ (Å) | 5.0489(1) | 5.0531(2) | 5.0589(1) |
| $V$ (Å$^3$) | 128.704(8) | 129.025(15) | 129.470(8) |
| $Z$ | 1 | 1 | 1 |
| Dimens min/mid/max(mm$^3$) | 0.04/0.06/0.10 | 0.04/0.06/0.10 | 0.04/0.06/0.10 |
| Calcd density (g·cm$^{-3}$) | 5.725 | 5.710 | 5.691 |
| Abs coeff (mm$^{-1}$) | 24.420 | 24.359 | 24.275 |
| $h$ | $-6 \le h \le 6$ | $-7 \le h \le 7$ | $-6 \le h \le 6$ |
| $k$ | $-6 \le k \le 6$ | $-7 \le k \le 7$ | $-6 \le k \le 6$ |
| $l$ | $-6 \le l \le 6$ | $-7 \le l \le 5$ | $-5 \le l \le 6$ |
| Reflns collected/unique/$R$(int) | 2383/53/0.0689 | 1633/63/0.0516 | 1550/53/0.0552 |
| Data/params/restraints | 53/5/0 | 63/5/0 | 53/5/0 |
| GOF on $F^2$ | 1.340 | 1.304 | 1.299 |
| $R$ indices (all data) ($R1/wR2$)[a] | 0.0472/0.0962 | 0.0441/0.0904 | 0.0486/0.0982 |
| Atom | La/Al | La/Al | La/Al |
| Site | $3c/1a$ | $3c/1a$ | $3c/1a$ |
| $x/a$ | 0/0 | 0/0 | 0/0 |
| $y/b$ | 0.5/0 | 0.5/0 | 0.5/0 |
| $z/c$ | 0.5/0 | 0.5/0 | 0.5/0 |
| $U_{\rm eq}$ (A$^2$) | 0.0041(12)/0.007(4) | 0.0046(8)/0.006(3) | 0.0107(12)/0.013(5) |

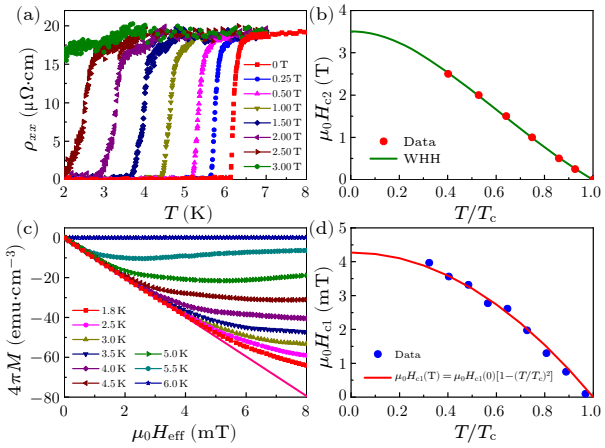


**Fig. 2.** (a) $\rho_{xx}(T)$ as a function of temperature at various magnetic fields up to 3 T. (b) Temperature dependence of $\mu_0 H_{c2}(T)$. The green line represents the fit using the WHH formula. (c) Low-field parts of $4\pi M(\mu_0 H_{\rm eff})$ curves at various temperatures below $T_c$. The pink line is the Meissner line. (d) Temperature dependence of $\mu_0 H_{c1}(T)$. The red line is the fit using the formula $\mu_0 H_{c1}(T) = \mu_0 H_{c1}(0)[1-(T/T_c)^2]$.

$\mu_0 H_{c2}(T)$ was determined using the criterion of 50% of the normal-state resistivity just above the superconducting transition, as shown in Fig. 2(b). It can be seen that $\mu_0 H_{c2}(T)$ increases with decreasing temperature with a slope $\frac{d\mu_0 H_{c2}}{dT}|_{T=T_c^{\rm onset}(0)} = -0.57\,{\rm T\cdot K^{-1}}$, where $T_c^{\rm onset}(0)$ is the superconducting transition temperature at zero field. Moreover, $\mu_0 H_{c2}(T)$ can be fitted well using the Werthamer-Helfand-Hohenberg (WHH) model [61] and the obtained value of $\mu_0 H_{c2}(0)$ is 3.5(1) T. This value is smaller than that of hexagonal $La_3Al$ ($\mu_0 H_{c2}(0) = 6.95$ T).[36] As the Pauli limiting field $\mu_0 H_{c2}^P(0) = 1.84 T_c = 10.96$ T [62] is significantly larger than $\mu_0 H_{c2}(0)$, the orbital-depairing mechanism should be dominant in $La_3Al$. Using the fitted $\mu_0 H_{c2}(0)$, the calculated Ginzburg-Landau coherence length $\xi_{\rm GL}(0)$ from the equation $\xi_{\rm GL} = \sqrt{\Phi_0/2\pi\mu_0 H_{c2}}$ ($\Phi_0 = h/2e$ is quantum flux) is 97.1(4) Å.

Figure 2(c) shows the low-field $M(\mu_0 H_{\rm eff})$ curves at various temperatures below $T_c$. $\mu_0 H_{\rm eff}$ was calculated by considering the demagnetization effect using the formula $\mu_0 H_{\rm eff} = \mu_0 H_a - NM$, where $N$ is the demagnetization factor and $\mu_0 H_a$ is the external field.[63] The estimated demagnetization factor was 0.38 and the fitted slope of $M(\mu_0 H_{\rm eff})$ curve at 1.8 K was −0.993(2), which is very close to −1 ($4\pi M = -\mu_0 H_{\rm eff}$). Thus, the full Meissner shielding effect in our measurements provides a reliable method for determining the value of $\mu_0 H_{c1}$. $\mu_0 H_{c1}$ is determined as the point deviating from linearity based on the criterion $\Delta 4\pi M = (4\pi M_m - 4\pi M_{th}) = 1\times10^{-6}$ emu·cm$^{-3}$, where $4\pi M_m$ is the measured moment value and $4\pi M_{th}$ is the calculated moment value in the same field. The $\mu_0 H_{c1}(T)$ values obtained at different temperatures are shown in Fig. 2(d). The $\mu_0 H_{c1}(T)$ can be fitted well using the formula $\mu_0 H_{c1}(T) = \mu_0 H_{c1}(0)[1-(T/T_c)^2]$ (red solid line) and the obtained $\mu_0 H_{c1}(0)$ is 4.3(1) mT. Similar to $\mu_0 H_{c2}(0)$, the value of $\mu_0 H_{c1}(0)$ for cubic $La_3Al$ is smaller than that for hexagonal $La_3Al$ ($\mu_0 H_{c1}(0) = 22.17$ mT).[36] According to the equation $\mu_0 H_{c1} = \frac{\Phi_0}{4\pi\lambda_{\rm GL}^2}\ln\frac{\lambda_{\rm GL}}{\xi_{\rm GL}}$, the value of superconducting penetration depth $\lambda_{\rm GL}(0)$ is 3738(53) Å. The determined Ginzburg-Landau constant $\kappa_{\rm GL}(=\lambda_{\rm GL}/\xi_{\rm GL})$ is 38.5(3), further confirming that $La_3Al$ is a type-II superconductor.

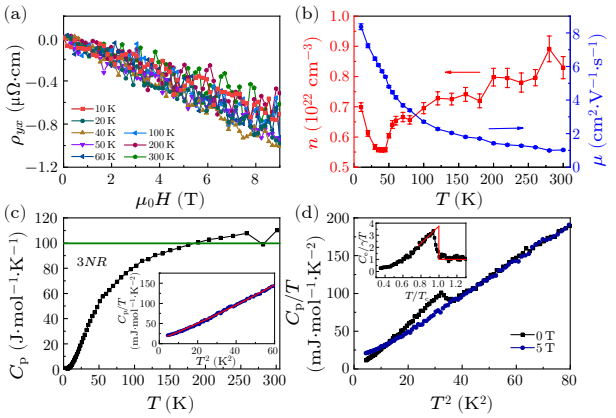


**Fig. 3.** (a) Field dependence of $\rho_{yx}(\mu_0 H)$ at various temperatures. (b) Temperature dependence of derived $n(T)$ and $\mu(T)$. (c) Temperature dependence of $C_p$ from 2 K to 300 K at zero field. Inset: $C_p/T$ vs. $T^2$ at 5 T. The red solid line represents the fit using the formula $C_P/T = \gamma + \beta T^2 + \delta T^4$. (d) Low-temperature specific heat $C_p/T$ vs. $T^2$ at zero field and 5 T. The Inset shows the relationship between $C_e/\gamma T$ and $T/T_c$.

Figure 3(a) shows the field dependence of the Hall resistivity $\rho_{yx}(\mu_0 H)$ at various temperatures. All curves display a negative slope, suggesting that the electron-type carriers play a dominant role in the transport of $La_3Al$. Using the linear fits of the $\rho_{yx}(\mu_0 H)$ curves and combining the results of $\rho_{xx}(T)$ at zero field, the carrier concentration $n(T)$ (red squares) and carrier mobility $\mu(T)$ (blue circles) as functions of temperature can be obtained. As depicted in Fig. 3(b), as the temperature decreases from 300 K to 60 K, $n(T)$ decreases slightly from approximately 0.83(4) to 0.65(1) × $10^{22}$ cm$^{-3}$. On further lowering of the temperature, it exhibits a sudden drop at approximately 55 K, which is in line with the anomaly in the $\rho_{xx}(T)$ curve. At lower temperatures, $n(T)$ increases to 0.70(2) × $10^{22}$ cm$^{-3}$ at 10 K. Moreover, $\mu(T)$ exhibited a gradual increase from 1.0(1) cm$^2$·V$^{-1}$·s$^{-1}$ at 300 K to 8.4(2) cm$^2$·V$^{-1}$·s$^{-1}$ at 10 K, and there was no obvious anomaly at $T \sim 55$ K. Figure 3(c) shows the specific heat $C_p(T)$ of $La_3Al$ measured from 2 K to 300 K at zero field. The value of $C_p(T)$ at 300 K approaches the classical value of $3NR$ ($\sim 99.77$ J·mol$^{-1}$·K$^{-1}$), as predicted by the Dulong-Petit law (green solid line), where $N$ (= 4) is the atomic number and $R$ (= 8.314 J·mol$^{-1}$·K$^{-1}$) is the ideal gas constant. In addition, there was a small kink near $T = 55$ K, which may be associated with the resistivity anomaly. Figure 3(d) shows the relationship between $C_p/T$ and $T^2$ in the low-temperature region, with $\mu_0 H = 0$ T and 5 T. It can be seen that there is a jump at $T_c \sim 6.06$ K for the curve measured at zero field, confirming the bulk superconducting transition in cubic $La_3Al$. $T_c$ agreed with the values obtained from the resistivity and magnetization measurements. By contrast, a field of 5 T completely suppressed the superconducting transition at $T > 2$ K. Moreover, the $C_P/T$ curve at 5 T can be fit-

ted using the formula $C_{\rm P}(T)/T = \gamma + \beta T^2 + \delta T^4$ [inset of Fig. 3(c)], where $\gamma$ is the electronic specific heat coefficient and $\beta$ and $\delta$ are the lattice-specific heat coefficients. The fitted $\gamma$ was 9.9(6) mJ·mol$^{-1}$·K$^{-2}$ when the values of $\beta$ and $\delta$ were 1.9(1) mJ·mol$^{-1}$·K$^{-4}$ and 0.006(1) mJ·mol$^{-1}$·K$^{-6}$. Correspondingly, the calculated Debye temperature $\Theta_{\rm D}$ is 160(1) K using the equation $\Theta_{\rm D} = (12\pi^4 NR/5\beta)^{1/3}$. The inset of Fig. 3(d) plots $C_{\rm e}/\gamma T$ versus $T/T_{\rm c}$, where $C_{\rm e}$ is the electronic specific heat, which is obtained by subtracting the lattice contribution from the total specific heat. The extracted specific heat jump $\Delta C_{\rm e}/\gamma T$ at $T_{\rm c}$ was approximately 2.20, which is larger than that of the BCS superconductor (1.43). This indicates that $La_3Al$ exhibits superconductivity with an intermediate coupling strength. In contrast, the EPC constant $\lambda_{\rm e-ph}$ is obtained from the McMillan equation [64]

$$\lambda_{\rm e-ph} = \frac{\mu^* \ln(1.45T_{\rm c}/\Theta_{\rm D}) - 1.04}{1.04 + \ln(1.45T_{\rm c}/\Theta_{\rm D})(1 - 0.62\mu^*)}. \quad (6)$$

When assuming the Coulomb pseudopotential $\mu^* \approx 0.13$, the value of $\lambda_{\rm e-ph}$ was determined to be 0.88(1) using $T_{\rm c} = 6.3$ K and $\Theta_{\rm D} = 160(1)$ K, which confirmed the intermediately coupled BCS superconductivity of $La_3Al$. [65]

Figure 4(a) shows the electronic band structure and partial DOS (PDOS) of $La_3Al$ calculated without spin-orbital coupling (SOC). There are three bands labeled *i*, *ii*, and *iii* crossing the Fermi level $E_{\rm F}$, among which there are short flat bands along the R-M path of the BZ. Based on orbital analysis, these short flat bands are dominated by La 5*d* electrons and IAEs [Fig. S1 in the Supplementary Material]. According to the PDOS in Fig. 4(a), the electronic states near $E_{\rm F}$ are mainly contributed to by the La 5*d* orbitals and IAEs, which are consistent with the band features. More importantly, a van Hove singularity exists around $E_{\rm F}$, resulting in a high DOS of 1.60 states/eV per atom at $E_{\rm F}$. The Fermi surface (FS) sheets for bands *i*, *ii*, and *iii* are shown in Fig. 4(b), where the Fermi velocities are displayed with color scales and the red and blue colors represent the highest and zero Fermi velocities, respectively. Clearly, the two FS sheets of bands *ii* and *iii* have lower Fermi velocities around the *M* point, which is favorable for a strong EPC. [65,66] Moreover, we also examined the electronic structure with the inclusion of SOC, but found that both the energy dispersion and the total DOS near $E_{\rm F}$ are approximately unchanged (Fig. S2).

To better understand the superconducting properties of $La_3Al$, we performed EPC calculations. The calculated total EPC constant $\lambda$ was 1.29, which is slightly larger than the experimental value. This leads to a superconducting $T_{\rm c}$ of 7.37 K based on the McMillan-Allen-Dynes formula [Eq. (4)]. After further consideration of the SOC, $\lambda$ was reduced to 1.28 and logarithmic phonon frequency increased from 53.85 cm$^{-1}$ to 58.52 cm$^{-1}$. The decrease in $\lambda$ and increase in $\omega_{\log}$ led to a slight change in $T_{\rm c}$ to 6.78 K, which is in good agreement with the measured value [Fig. 1(d)]. From the momentum- and mode-resolved EPC parameter $\lambda_{\boldsymbol{q}\nu}$ [Fig. 4(c)], we learn that the largest contribution comes from the acoustic branches around the *X* and *Γ* points, which results in two high peaks (around 44 cm$^{-1}$ and 72 cm$^{-1}$) in the Eliashberg spectral function $\alpha^2F(\omega)$ [the top part of Fig. 4(d)]. By combining the frequency-dependent EPC parameters $\lambda(\omega)$ and phonon density of states (PHDOS) [Fig. 4(d)], it can be seen that La vibrations play a dominant role in superconductivity. Specifically, the strongest EPC was located at the softened acoustic branch at *X* point and was related to the $A_{2u}$ mode [Fig. 4(c)]. This mode corresponds to the vibrations of the La atoms in the La-Al layers along the *c*-axis [Fig. S3(a)]. We found that when the La atoms had small displacements along the normal mode coordinates of the $A_{2u}$ mode, and there were noticeable shifts in the electronic bands around the Fermi level at the *M* point [Fig. S3(b)], whose orbital weights were derived from the IAEs and La 5*d* electrons (Fig. S1). These electronic band shifts indicate that the $A_{2u}$ phonons coupled strongly with these electronic states. In summary, we propose that the superconducting pairing in $La_3Al$ belongs to the conventional BCS type and that the superconductivity originates from the coupling of the electronic states of La 5*d* and IAEs with La-derived low-frequency phonons.

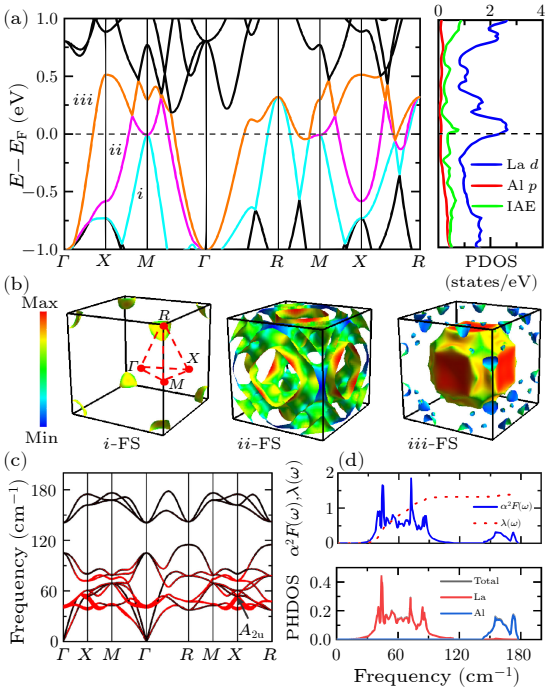


**Fig. 4.** (a) The orbital-resolved electronic band structure and PDOS of $La_3Al$. (b) The Fermi-velocity-projected FS sheets corresponding to the bands *i*, *ii*, and *iii* in (a), respectively. (c) Phonon dispersion curves. The size of red dots represents the EPC strength $\lambda_{\boldsymbol{q}\nu}$. (d) The Eliashberg spectral function $\alpha^2F(\omega)$, frequency-dependent EPC constant $\lambda(\omega)$, and phonon density of states (PHDOS).

*4. Conclusion.* In summary, cubic $La_3Al$ single crystals were grown successfully using an La flux, and their physical properties and electronic structures were investigated in detail. Bulk superconductivity with $T_{\rm c}^{\rm onset} = 6.32$ K was observed from electrical resistivity, magnetization, and specific heat measurements. Further analysis revealed that cubic $La_3Al$ is an intermediately coupled type-II BCS superconductor. Moreover, cubic $La_3Al$ can host IAEs and can thus be considered an electride super-

conductor, similar to cubic $La_3In$. This study deepens the understanding of electride superconducting materials.

*Acknowledgements.* This work was supported by the National Key R&D Program of China (Grant Nos. 2022YFA1403800, 2023YFA1406500, and 2022YFA1403103), the National Natural Science Foundation of China (Grant Nos. 12274459, 12174443, 12074013, and 12404266), and the Science Research Project of Hebei Education Department (Grant No. BJ2025060). Computational resources were provided by the Physical Laboratory of High-Performance Computing at Renmin University of China.

# References

[1] Dye J L 2009 *Acc. Chem. Res.* **42** 1564
[2] Dye J L 2003 *Science* **301** 607
[3] Miao M S and Hoffmann R 2014 *Acc. Chem. Res.* **47** 1311
[4] Toda Y, Yanagi H, Ikenaga E, Kim J J, Kobata M, Ueda S, Kamiya T, Hirano M, Kobayashi K, and Hosono H 2007 *Adv. Mater.* **19** 3564
[5] Lee K, Kim S W, Toda Y, Matsuishi S, and Hosono H 2013 *Nature* **494** 336
[6] Zhang X, Xiao Z W, Lei H C, Toda Y, Matsuishi S, Kamiya T, Ueda S, and Hosono H 2014 *Chem. Mater.* **26** 6638
[7] Xu H L, Li Z R, Wu D, Wang B Q, Li Y, Gu F L, and Aoki Y 2007 *J. Am. Chem. Soc.* **129** 2967
[8] Phillips R C, Pratt W P, and Dye J L 2000 *Chem. Mater.* **12** 3642
[9] Kim Y J, Kim S M, Yu C, Yoo Y, Cho E J, Yang J W, and Kim S W 2017 *Langmuir* **33** 954
[10] Kitano M, Inoue Y, Yamazaki Y, Hayashi F, Kanbara S, Matsuishi S, Yokoyama T, Kim S W, Hara M, and Hosono H 2012 *Nat. Chem.* **4** 934
[11] Kang S H, Bang J, Chung K, Nandadasa C N, Han G, Lee S, Lee K H, Lee K, Ma Y, Oh S H, Kim S G, Kim Y M, and Kim S W 2020 *Sci. Adv.* **6** eaba7416
[12] Kim K B, Kikuchi M, Miyakawa M, Yanagi H, Kamiya T, Hirano M, and Hosono H 2007 *J. Phys. Chem. C* **111** 8403
[13] Hu J, Xu B, Yang S A, Guan S, Ouyang C, and Yao Y 2015 *ACS Appl. Mater. Interfaces* **7** 24016
[14] Lee S Y, Hwang J Y, Park J, Nandadasa C N, Kim Y, Bang J, Lee K, Lee K H, Zhang Y, Ma Y, Hosono H, Lee Y H, Kim S G, and Kim S W 2020 *Nat. Commun.* **11** 1526
[15] Hirayama M, Matsuishi S, Hosono H, and Murakami S 2018 *Phys. Rev. X* **8** 031067
[16] Zhao Z, Zhang S, Yu T, Xu H, Bergara A, and Yang G 2019 *Phys. Rev. Lett.* **122** 097002
[17] Liu Z, Zhuang Q, Tian F, Duan D, Song H, Zhang Z, Li F, Li H, Li D, and Cui T 2021 *Phys. Rev. Lett.* **127** 157002
[18] Liu Z, Duan D, Zhuang Q, and Cui T 2023 *Phys. Rev. B* **108** L100507
[19] Hou J, Dong X, Oganov A R, Weng X J, Hao C M, Yang G, Wang H T, Zhou X F, and Tian Y 2022 *Phys. Rev. B* **106** L220501
[20] Zhao Y, Bergara A, Zhang X, Li F, Liu Y, and Yang G 2023 *Phys. Rev. B* **108** 104505
[21] Guo Z, Bergara A, Zhang X, Li X, Ding S, and Yang G 2024 *Phys. Rev. B* **109** 134505
[22] You J Y, Gu B, Su G, and Feng Y P 2022 *J. Am. Chem. Soc.* **144** 5527
[23] Huang H M, Zhu Q, Blatov V A, Oganov A R, Wei X, Jiang P, and Li Y L 2023 *Nano Lett.* **23** 5012
[24] Wan Z, Zhang C, Yang T, Xu W, and Zhang R 2022 *New J. Phys.* **24** 113012
[25] Zhang X, Yao Y, Ding S, Bergara A, Li F, Liu Y, Zhou X F, and Yang G 2023 *Phys. Rev. B* **107** L100501
[26] Wang Q, Zhang S, Li H, Wang H, Liu G, Ma J, Xu H, Liu H, and Ma Y 2023 *J. Mater. Chem. A* **11** 21345
[27] Shimizu K, Ishikawa H, Takao D, Yagi T, and Amaya K 2002 *Nature* **419** 597
[28] Struzhkin V V, Eremets M I, Gan W, Mao H K, and Hemley R J 2002 *Science* **298** 1213
[29] Hosono H, Kim S W, Matsuishi S, Tanaka S, Miyake A, Kagayama T, and Shimizu K 2015 *Philos. Trans. R. Soc. A* **373** 20140450
[30] Matsuishi S, Toda Y, Miyakawa M, Hayashi K, Kamiya T, Hirano M, Tanaka I, and Hosono H 2003 *Science* **301** 626
[31] Miyakawa M, Kim S W, Hirano M, Kohama Y, Kawaji H, Atake T, Ikegami H, Kono K, and Hosono H 2007 *J. Am. Chem. Soc.* **129** 7270
[32] Zhang Y, Wang B, Xiao Z, Lu Y, Kamiya T, Uwatoko Y, Kageyama H, and Hosono H 2017 *npj Quantum Mater.* **2** 45
[33] Tu Z, Sun P, Ma P, Zhen H, Tian S, Wang S, Cui T, Liu Z, Liu K, and Lei H 2024 arXiv:2410.10443 [cond-mat.supr-con]
[34] Bucher E, Maita J P, and Cooper A S 1972 *Phys. Rev.* **6** 2709
[35] Garde C S, Ray J, and Chandra G 1993 *J. Alloys Compd.* **198** 165
[36] Yu Y, Liu Z, Chen Z, Li Q, Wang Y, Wang X, Gong C, Zhuang Z, Ruan B, Ren H, Sun P, Guo J, and Jin S 2025 *Chin. Phys. B* **34** 017401
[37] Chen Y Y, Yao Y D, Hu B C, Jang C H, Lawrence J M, Huang H, and Li W H 1997 *Phys. Rev. B* **55** 5937
[38] Peng D, Zhan Y, She J, Pang M, and Du Y 2010 *J. Alloys Compd.* **507** 62
[39] Blöchl P E 1994 *Phys. Rev. B* **50** 17953
[40] Kresse G and Joubert D 1999 *Phys. Rev. B* **59** 1758
[41] Kresse G and Hafner J 1993 *Phys. Rev. B* **47** 558
[42] Kresse G and Furthmüller J 1996 *Comput. Mater. Sci.* **6** 15
[43] Kresse G and Furthmüller J 1996 *Phys. Rev. B* **54** 11169
[44] Perdew J P, Burke K, and Ernzerhof M 1996 *Phys. Rev. Lett.* **77** 3865
[45] Marzari N, Mostofi A A, Yates J R, Souza I, and Vanderbilt D 2012 *Rev. Mod. Phys.* **84** 1419
[46] Mostofi A A, Yates J R, Pizzi G, Lee Y S, Souza I, Vanderbilt D, and Marzari N 2014 *Comput. Phys. Commun.* **185** 2309
[47] Kawamura M 2019 *Comp. Phys. Commun.* **239** 197
[48] Baroni S, de Gironcoli S, Dal Corso A, and Giannozzi P 2001 *Rev. Mod. Phys.* **73** 515
[49] Giustino F 2017 *Rev. Mod. Phys.* **89** 015003
[50] Giannozzi P, Baroni S, Bonini N, Calandra M, Car R, Cavazzoni C, Ceresoli D, Chiarotti G L, Cococcioni M, Dabo I *et al.* 2009 *J. Phys. Condens. Matter* **21** 395502
[51] Rappe A M, Rabe K M, Kaxiras E, and Joannopoulos J D 1990 *Phys. Rev. B* **41** 1227
[52] Dal Corso A 2014 *Comput. Mater. Sci.* **95** 337
[53] https://www.quantum-espresso.org/pseudopotentials.
[54] Eliashberg G M 1960 *Sov. Phys. JETP* **11** 696
[55] Allen P B 1972 *Phys. Rev. B* **6** 2577
[56] Park C, Kim S W, and Yoon M 2018 *Phys. Rev. Lett.* **120** 026401
[57] Hosono H and Kitano M 2021 *Chem. Rev.* **121** 3121
[58] Kim H, Park I, Shim J H, and Kim D Y 2024 *npj Comput. Mater.* **10** 173
[59] Dye J L 1990 *Science* **247** 663
[60] Werthamer N R, Helfand E, and Hohenberg P C 1966 *Phys. Rev.* **147** 295
[61] Maki K 1966 *Phys. Rev.* **148** 362
[62] Aharoni A 1998 *J. Appl. Phys.* **83** 3432
[63] McMillan W L 1968 *Phys. Rev.* **167** 331
[64] Allen P B and Dynes R C 1975 *Phys. Rev. B* **12** 905
[65] Zhang X, Zhao M, and Liu F 2019 *Phys. Rev. B* **100** 104527
[66] An J M, and Pickett W E 2001 *Phys. Rev. Lett.* **86** 4366